Supporting Information

Spin polarized oxygen evolution reaction in chiral amorphous manganese-doped cobalt oxide: Enhancing electrocatalytic activity via lattice oxygen participation

Tae Hyung Kim [a], Hyeon Keun Cho [a], Seung Hyun Jae [a], Su Hwan Lee [a], Jeongu You [b], Youn Jeong Jang [b], Bongjun Yeom [b], Young Moo Lee [a,] and Young-Hoon Kim [a,]**

[a] Department of Energy Engineering, Hanyang University, 222 Wangsimni-ro, Seongdong-gu, Seoul 04763, Republic of Korea

[b] Department of Chemical Engineering, Hanyang University, 222 Wangsimni-ro, Seongdong-gu, Seoul 04763, Republic of Korea

***Corresponding Author:** ymlee@hanyang.ac.kr, younghoonkim@hanyang.ac.kr

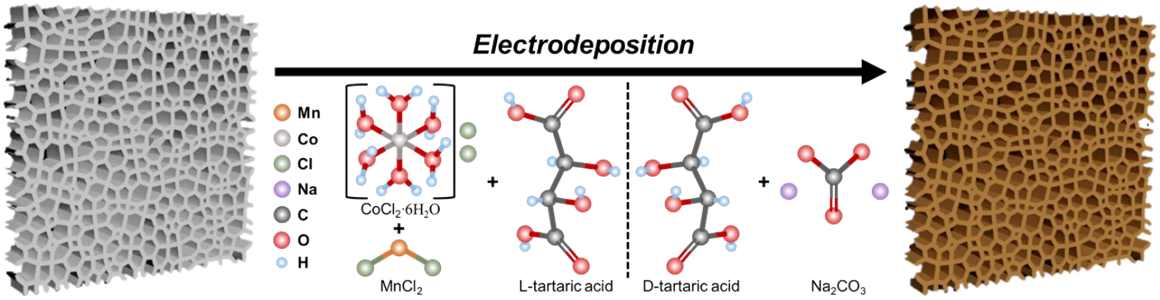

Fig. S1 Schematic illustration of the direct electrodeposition of chiral amorphous manganese-doped cobalt oxide (Mn:CoO_x) on Ni foam.

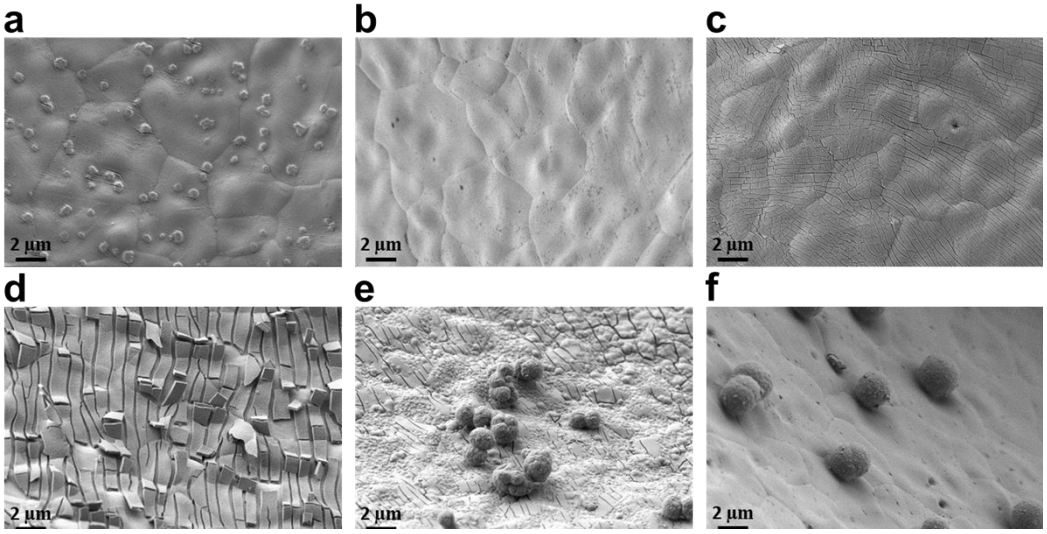

Fig. S2 Scanning electron microscopy (SEM) images of (a) *L*-CoO_x, (b) *L*-$Mn_{0.2}$:$Co_{0.8}O_x$, (c) *L*-$Mn_{0.25}$:$Co_{0.75}O_x$, (d) *L*-$Mn_{0.4}$:$Co_{0.6}O_x$, (e) *L*-$Mn_{0.6}$:$Co_{0.4}O_x$ and (f) *L*-MnO_x.

\

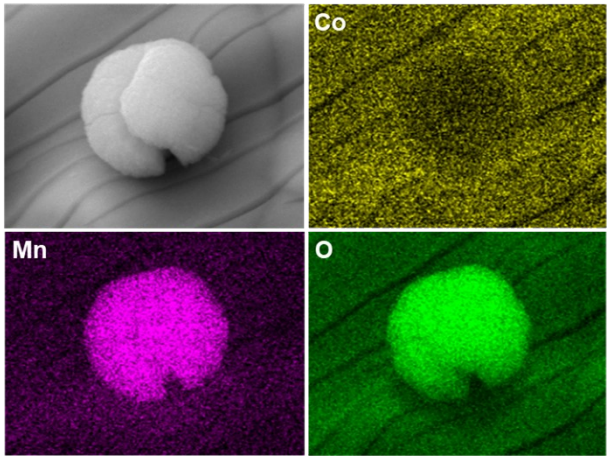

Fig. S3 SEM image and elemental mapping (Co, Mn and O) of *L*-$Mn_{0.6}$:$Co_{0.4}O_x$.

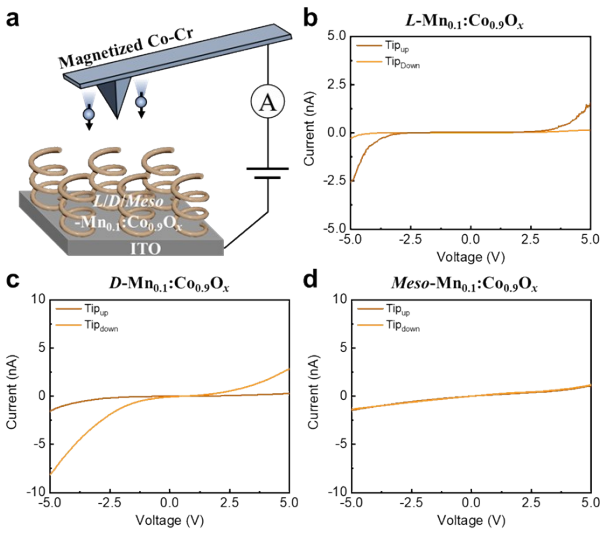

Fig. S4 (a) Schematic diagram of the magnetic conductive probe atomic force microscopy (mCP-AFM) used for thin film measurements. Spin-polarized average *I-V* curves of chiral (b) *L*-$Mn_{0.1}$:$Co_{0.9}O_x$, (c) *D*-$Mn_{0.1}$:$Co_{0.9}O_x$ and (d) achiral *meso*-$Mn_{0.1}$:$Co_{0.9}O_x$.

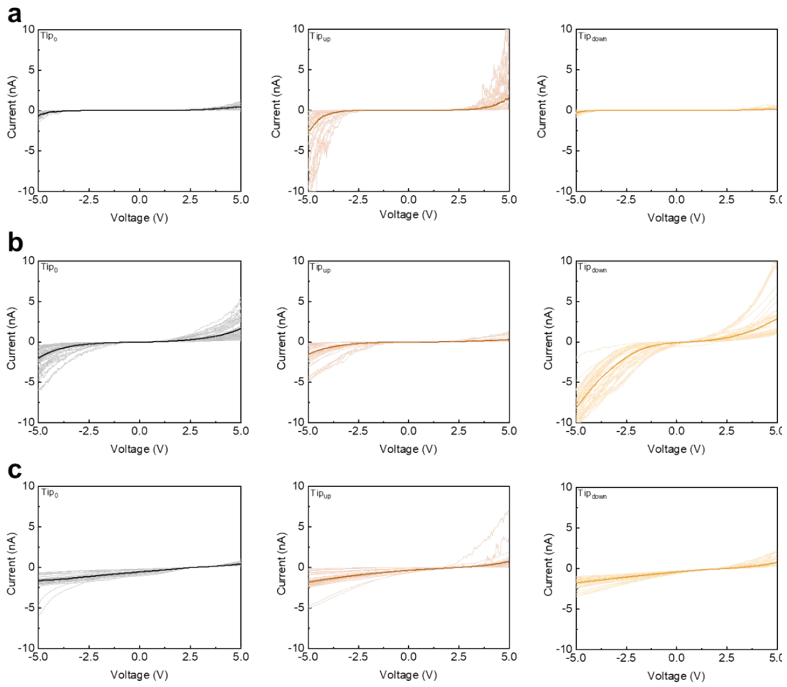

Fig. S5 Raw and averaged (bold) *I-V* curves of chiral (a) *L*-$Mn_{0.1}$:$Co_{0.9}O_x$, (b) *D*-$Mn_{0.1}$:$Co_{0.9}O_x$ and (c) achiral *meso*-$Mn_{0.1}$:$Co_{0.9}O_x$ thin films, measured using mCP-AFM over a voltage range of -5 V to 5 V. Measurements were conducted with a non-magnetized tip (black), a tip magnetized upward (brown) and a tip magnetized downward (orange).

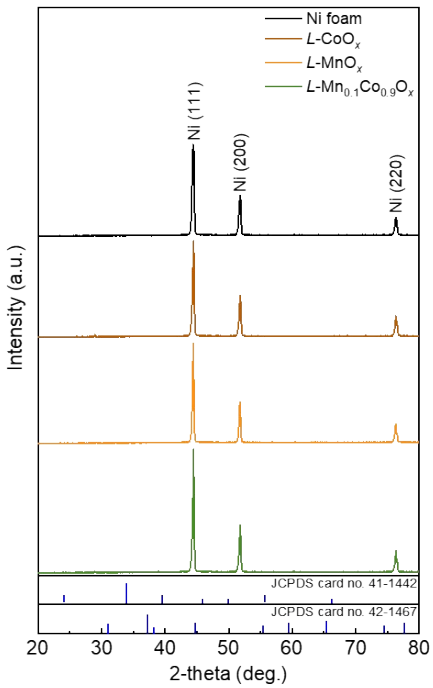

Fig. S6 XRD peaks of Ni foam, *L*-CoO_x electrodeposited on Ni foam, *L*-MnO_x electrodeposited on Ni foam and *L*-$Mn_{0.1}$:CoO_x electrodeposited on Ni foam.

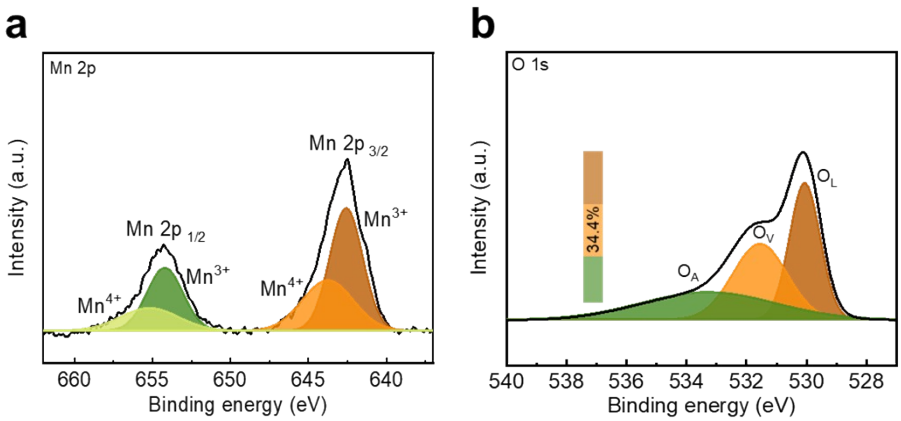

Fig. S7 X-ray photoelectron spectroscopy (XPS) spectra of *L*-MnO_x thin film (a) Mn 2p and (b) O 1s peaks.

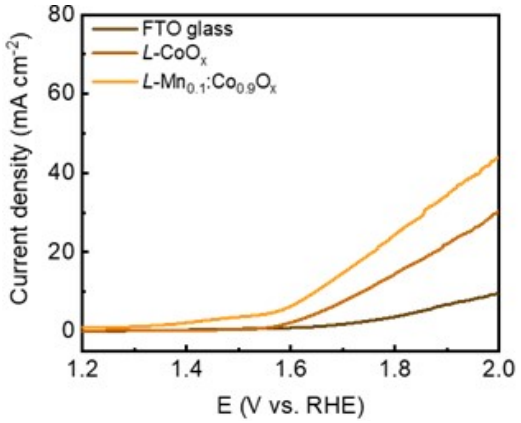

Fig. S8 LSV curves of bare FTO, *L*-CoO_x/FTO and *L*-$Mn_{0.1}$:$Co_{0.9}O_x$/FTO electrodes.

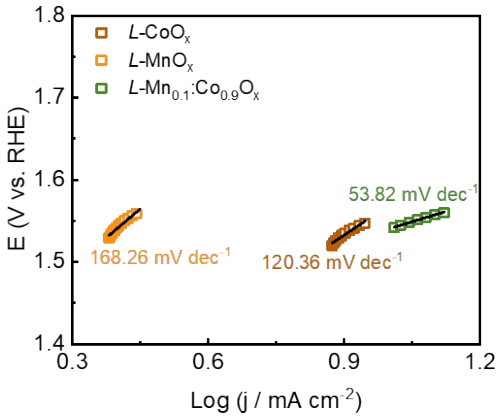

Fig. S9 Tafel plots of *L*-CoO_x, *L*-MnO_x and *L*-$Mn_{0.1}$:$Co_{0.9}O_x$ measured 1 M KOH under a half-cell configuration without *iR* compensation.

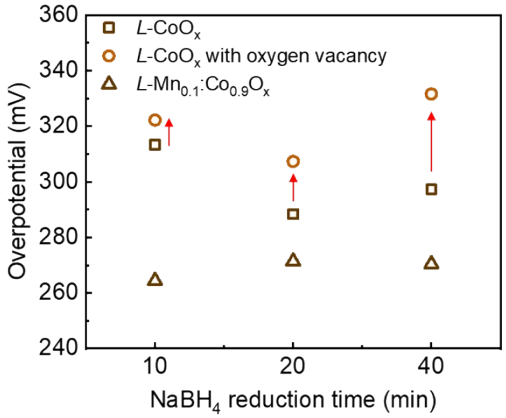

Fig. S10 Overpotential at 10 mA cm^{-2} for pristine and $NaBH_4$-reduced *L*-CoO_x with pristine *L*-$Mn_{0.1}$:$Co_{0.9}O_x$ as a function of reduction time in 0.5 M $NaBH_4$, measured for independently prepared samples.

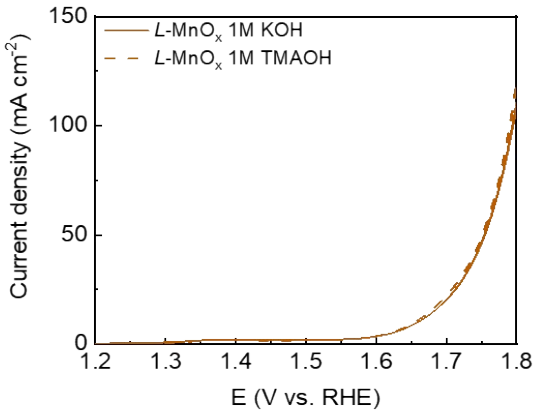

Fig. S11 LSV curves with 90% *iR* compensation of *L*-MnO_x in 1 M tetramethylammonium hydroxide (TMAOH).

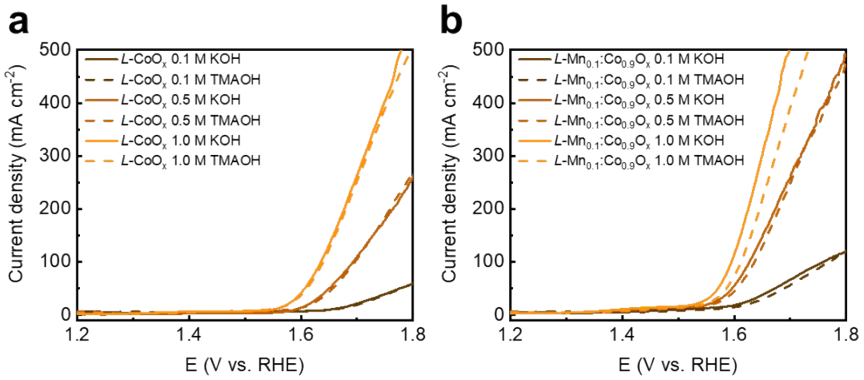

Fig. S12 LSV curves with 90% *iR* compensation of chiral (a) *L*-CoO_x and (b) *L*-$Mn_{0.1}$:$Co_{0.9}O_x$ in KOH and tetramethylammonium hydroxide (TMAOH) at different concentrations of 0.1, 0.5 and 1.0 M.

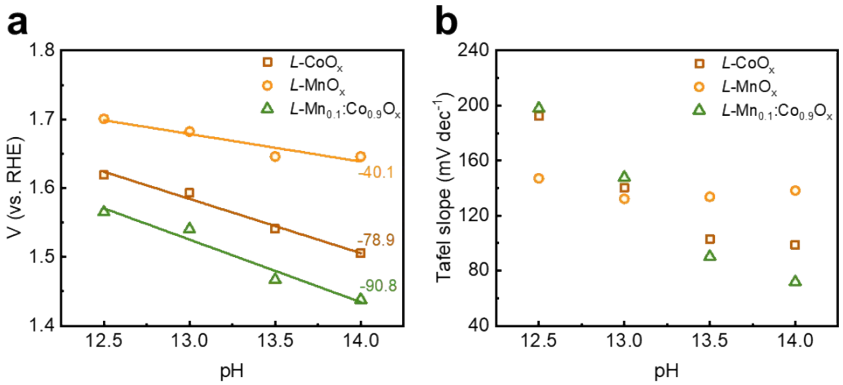

Fig. S13 (a) pH-dependent onset potential on RHE scale and (b) Tafel slope of *L*-CoO_x, *L*-MnO_x and *L*-$Mn_{0.1}$:$Co_{0.9}O_x$.

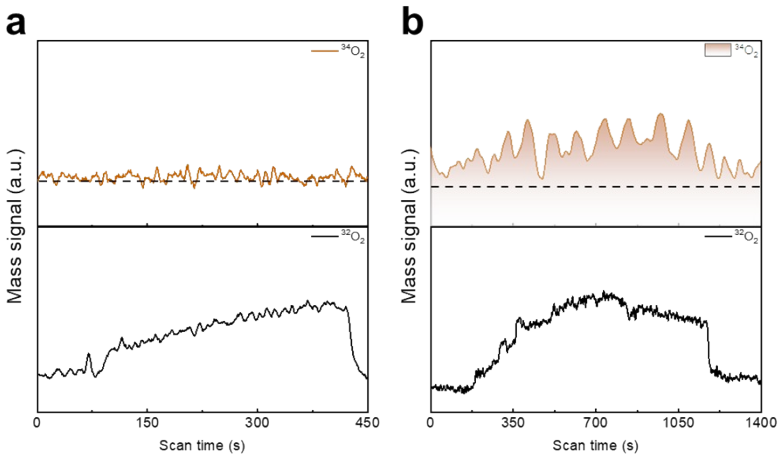

Fig. S14 DEMS signals corresponding to $^{34}O_2$ and $^{32}O_2$ evolution during the OER for (a) *L*-CoO_x and (b) *L*-$Mn_{0.1}$:$Co_{0.9}O_x$.

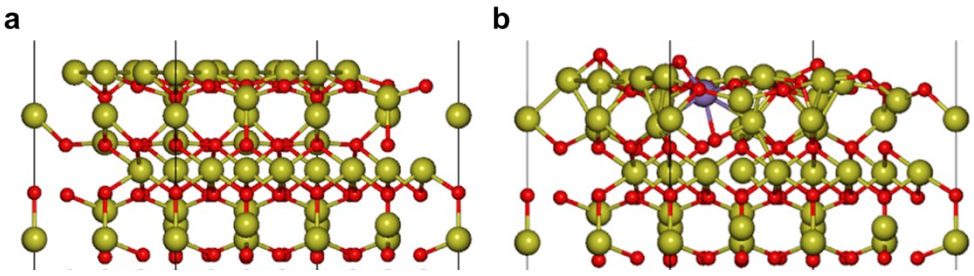

Fig. S15 Theoretical calculation models of (a) *L*-Co_3O_4 and (b) *L*-Mn:Co_3O_4 slabs.

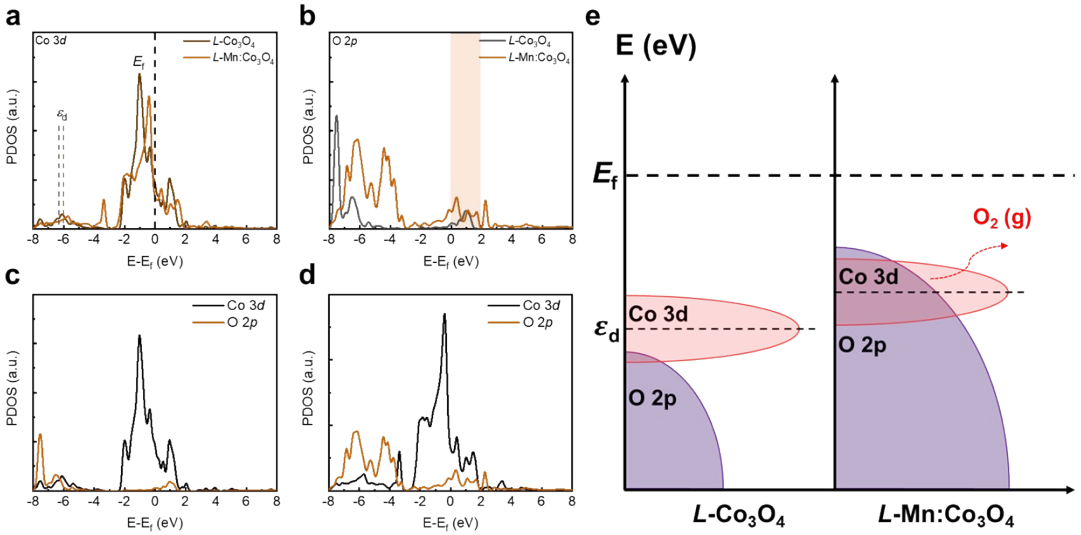

Fig. S16 DFT calculations of *L*-Co_3O_4 and *L*-Mn:Co_3O_4. Calculated PDOS of (a) Co 3*d* and (b) O 2*p* orbitals. Combined PDOS of Co 3*d* and O 2*p* orbitals for (c) *L*-Co_3O_4 and (d) *L*-Mn:Co_3O_4 slabs. (e) Schematic band diagrams of *L*-Co_3O_4 and *L*-Mn:Co_3O_4.

To further understand the electronic structure modulation induced by Mn incorporation, projected density of states (PDOS) calculations were performed using a representative Co_3O_4 (311) slab model with Mn substitution (Fig. S15†). As shown in Fig. S16a†, Mn incorporation shifts the Co d-band center (ε_d) closer to the Fermi level (E_f) from −6.31 eV to −5.97 eV, indicating enhanced hybridization between metal–oxygen interactions. In addition, the O 2*p* PDOS exhibits an increased population of states near and above the Fermi level after Mn doping (Fig. S16b†), which has been associated with enhanced oxygen redox activity and participation of lattice oxygen in catalytic reactions. Moreover, a more pronounced overlap between Co 3*d* and O 2*p* orbitals is observed upon Mn incorporation (Fig. S16c, d†), suggesting increased metal–oxygen covalency. In particular, increased M–O covalency and the presence of O 2*p* states near the Fermi level have been strongly correlated with the transition from the AEM to the LOM pathways (Fig. S16e†).[28-30] Therefore, these results suggest that Mn doping tunes the electronic structure toward a regime favorable for lattice oxygen participation by enhancing metal–oxygen covalency, increasing the availability of O 2*p* states near the Fermi level, facilitating oxygen vacancy formation and oxygen ion mobility.

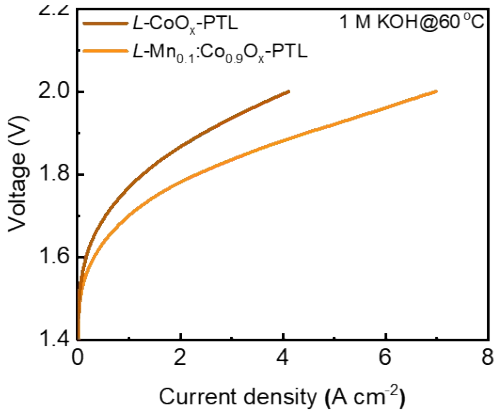

Fig. S17 Polarization curves of AEMWEs with *L*-CoO_x-PTL and *L*-$Mn_{0.1}$:$Co_{0.9}O_x$-PTL anodes measured in 1 M KOH at 60 ℃.

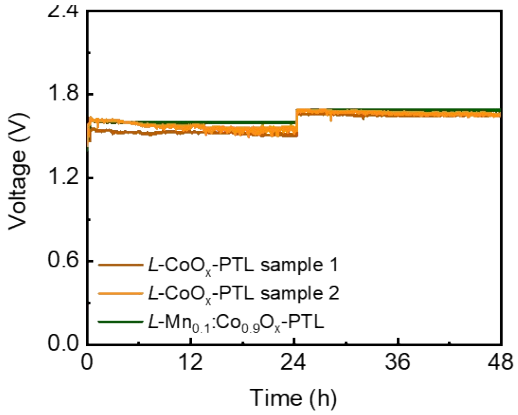

Fig. S18 Stabilization procedure prior to the durability test, involving current holds at 0.25 A cm^{-2} and 0.5 A cm^{-2} for 24 hours each, followed by operating at 1 A cm^{-2} for single-cell AEMWEs with *L*-CoO_x-PTL sample 1, sample 2 and *L*-$Mn_{0.1}$:$Co_{0.9}O_x$-PTL in 1 M KOH at 60 ℃.

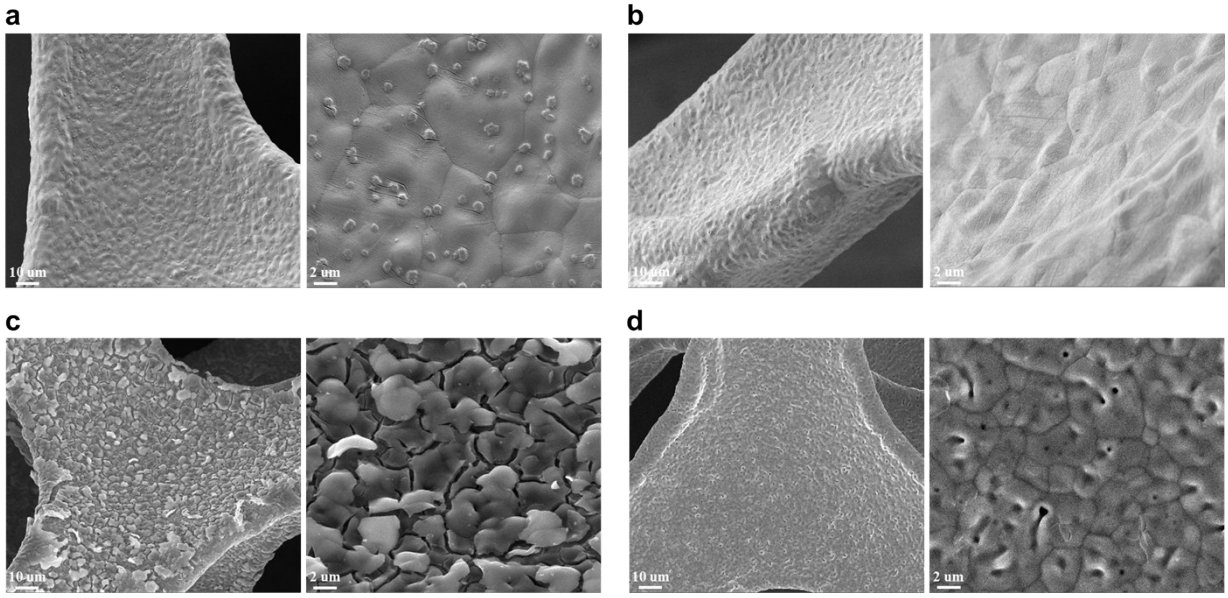

Fig. S19 SEM images of (a) *L*-CoO_x-porous transport layer (PTL) and (b) *L*-$Mn_{0.1}$:$Co_{0.9}O_x$-PTL before and (c) *L*-CoO_x-PTL and (d) *L*-$Mn_{0.1}$:$Co_{0.9}O_x$-PTL after 50 cyclic voltammetry (CV) cycles between 1 and 2 V (vs. RHE).

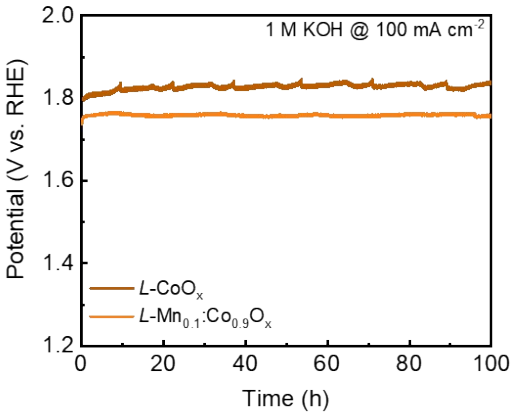

Fig. S20 Durability tests of *L*-CoO_x and *L*-$Mn_{0.1}$:$Co_{0.9}O_x$ at 100 mA cm^{-2} for 100 hours in a half-cell configuration.

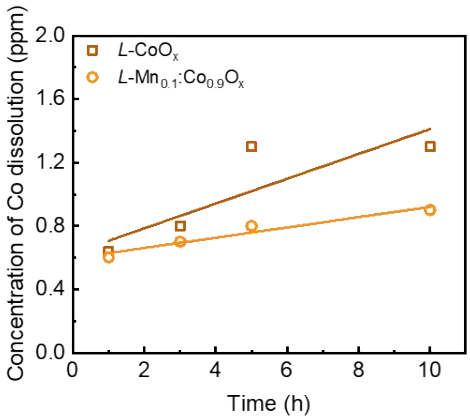

Fig. S21 Time-dependent Co dissolution during a 10 hour durability test at a constant current density of 500 mA cm^{-2} for *L*-CoO_x and *L*-$Mn_{0.1}$:$Co_{0.9}O_x$ in 1 M KOH.

Table S1. Summary of Mn fraction (Mn / (Mn + Co)) of chiral Mn:CoO_x samples determined by SEM-EDS.

Sample	Mn (at%)	Co (at%)	Mn / (Mn + Co) (%)
L-CoO_x	73.92	0	0.00
L-$Mn_{0.05}$:$Co_{0.95}O_x$	76.74	4.74	5.82
L-$Mn_{0.1}$:$Co_{0.9}O_x$	22.1	2.09	8.64
L-$Mn_{0.15}$:$Co_{0.85}O_x$	55.96	17.02	23.32
L-$Mn_{0.2}$:$Co_{0.8}O_x$	27.83	8.59	23.59
L-$Mn_{0.25}$:$Co_{0.75}O_x$	41.09	14.87	26.57
L-MnO_x	0	26.74	100.00

Table S2. Summary of overpotential (10mA cm^{-2} without *iR* compensation), double layer capacitance (C_{dl}) results for chiral amorphous *L*-Mn:CoO_x.

Sample	Overpotential (mV)	C_{dl} (mF cm^{-2})
L-CoO_x	327	1.32
L-$Mn_{0.05}$:$Co_{0.95}O_x$	319	1.53
L-$Mn_{0.1}$:$Co_{0.9}O_x$	266	1.64
L-$Mn_{0.15}$:$Co_{0.85}O_x$	309	1.57
L-$Mn_{0.2}$:$Co_{0.8}O_x$	313	1.47
L-$Mn_{0.25}$:$Co_{0.75}O_x$	318	1.63
L-MnO_x	426	9.9

Table S3. Summary of the reported properties of PGM-free AEMWEs

Anode catalyst	Cathode catalyst	Membrane	Electrolyte	Operation temperature (℃)	Current density (A cm^{-2} at V)	Ref.
$CuCo_2O_4$	Pt/C	X37-50	1 M KOH	45	1.4 (1.9)	4
N-doped CoO	Pt/C	piperION A15R	1 M KOH	60	2 (2.06)	5
$Ru_{8\%}$-Co_3O_4	Pt/C	FAA-3-PK-130	1 M KOH	85	1 (2.06)	6
Fe@Co	Pt/C	X37-50	1 M KOH	60	2.44 (1.8)	7
Fe-Ni-Co	PtRu/C	PSTP-20	1 M KOH	80	10.7 (2)	8
Fe-Ni-Co	PtRu/C	Patterned PDTP	1 M KOH	80	14.42 (2)	9
L-$Mn_{0.1}$:$Co_{0.9}O_x$-PTL	PtRu/C	PDTP-25	1 M KOH	80	11.14 (2)	Our work

Supplementary References

1 P. Ye, K. Fang, H. Wang, Y. Wang, H. Huang, C. Mo, J. Ning and Y. Hu, *Nat. Commun.*, 2024, **15**, 1012.
2 F. Wang, X. Xu, Y. Li, L. Gu, L. Li, H. Liu and H. Cong, *Appl. Catal. B Environ. Energy*, 2025, **363**, 124838.
3 B. Ge, P. Jiang, C. Huang, B. Chen and X. Qiu, *ACS Sustain. Chem. Eng.*, 2025, **13**, 20569-20579.
4 Y. S. Park, M. J. Jang, J. Jeong, S. M. Park, X. Wang, M. H. Seo, S. M. Choi and J. Yang, *ACS Sustainable. Chem. Eng.*, 2020, **8**, 2344-2349.
5 P.-C. Yu, X.-L. Zhang, T.-Y. Zhang, X.-Y.-N. Tao, T. Y. Yang, Y.-H. Wang, S.-C. Zhang, F.-Y. Gao, Z.-Z. Niu, M.-H. Fan and M.-R. Gao, *J. Am. Chem. Soc.*, 2024, **146**, 20379-20390.
6 FY. Zhou, Y. Mao, C. Ye, Z. Wang, S. Wei, J. V. Kennedy, Y. Zhao, H. Yang, B. C. C. Cowie and G. I. N. Waterhouse, *Adv. Energy Mater.*, 2025, 2500700.
7 S. Han, J. H. Ryu, W. B. Lee, J. Ryu and J. Yoon, *Small*, 2024, **20**, 2311052.
8 C. Hu, H. W. Kang, K. S. Jung, M.-L. Liu, Y. J. Lee, J. H. Park, N. Y. Kang, M.-G. Kim, S. J. Yoo, C. H. Park and Y. M. Lee, *Adv. Sci.*, 2024, **11**, 2306988.
9 C. Hu, Y. J. Lee, Y. Ma, X. Zhang, S. W. Jung, H. Hwang, H. K. Cho, M.-G. Kim, S. J. Yoo, Q. Zhang and Y. M. Lee, *ACS Energy Lett.*, 2024, **9**, 1219-1227.